Nanocarbons in different structural dimensions (0–3D) for phenol adsorption and metal-free catalytic oxidation

Stacey Indrawirawan, Hongqi Sun[*], Xiaoguang Duan, Shaobin Wang[*]

Department of Chemical Engineering, Curtin University, GPO Box U1987, Perth, WA 6845, Australia

ARTICLE INFO

ABSTRACT

Metal-free nanocarbon materials in different structural dimensions, such as 0D fullerene (C_{60}), 1D single-walled carbon nanotubes (SWCNTs), 2D graphene nanoplate (GNP), 3D hexagonally-ordered mesoporous carbon (CMK-3) and cubically-ordered mesoporous carbon (CMK-8) were investigated for adsorption and catalytic oxidation of phenol in water solutions. A variety of characterisation techniques were used to investigate the properties of the carbon samples. It was found that structural dimension and heat treatment would significantly affect the performance of the nanocarbons in adsorption and catalysis. Both GNP and CMK-3 showed better phenol adsorption with around 40% phenol removal in 500 mL of 20 ppm solutions. The nanocarbons were also used for metal-free activation of peroxymonosulfate (PMS) to produce sulfate radicals for catalytic phenol oxidation. Efficient catalysis was observed on CMK-3, CMK-8 and SWCNTs. Thermal treatment of the nanocarbons at 350 °C in nitrogen was conducted to modulate the crystal- and micro-structures and surface functional groups of the different nanocarbons. Enhancements at 2-fold in adsorption on SWCNTs and 7.5-fold in catalysis on CMK-8 were observed after the heat treatments. Mechanisms of adsorption and catalytic oxidation of phenol were discussed. This study contributes to the development of green materials for sustainable remediation of aqueous organic pollutants.

© 2015 Elsevier B.V. All rights reserved.

1. Introduction

Severe air, water and soil pollutions from the rapid developments in industrialisation, population expansion and urbanisation have posed detrimental effects on the eco-environment and human life [1]. Toxic gases, heavy metals, organics and bio-toxics are the major contributors to the pollutions. A variety of chemical, physical and biological treatments have been employed to tackle the issues [2], among which adsorption and catalytic oxidation processes have been proven to be most effective for removal of aqueous contaminants [3,4]. For efficient adsorption and degradation, many porous materials have been developed and employed [5]. Pillared clays, zeolites, mesoporous metal oxides, polymers and metal-organic frameworks have shown varying effectiveness in removing toxic pollutants [6]. However, most traditional adsorbents and catalysts are metal-based materials [7–10] and the demerits of high-cost, scarcity in nature and metal leaching of those materials were

experienced [11]. Metal-free carbon materials for adsorption and catalytic oxidation are expected to overcome the issues.

Carbonaceous-based adsorbents including activated carbon, carbon nanotubes (CNTs), fullerene (C_{60}), graphene oxide (GO), and graphene have demonstrated high adsorption capacities and thermal stabilities [12,13]. Also for catalytic oxidation, reduced graphene oxide (rGO) was recently demonstrated to be an effective catalyst for activation of peroxymonosulfate (PMS) [11], which was previously achieved only on homogeneous or heterogeneous metal-based catalysts [3,7,14–19]. Physical CO_2 activation at a high temperature and chemical activation using $ZnCl_2$ were applied to improve the porous structure and surface features of rGO samples, and enhanced adsorption and catalysis were then achieved [4,20]. It was suggested that three important parameters such as specific surface area (SSA), porous structure and specific functional groups can enhance the performance of the green catalysts [4,13,20–22].

Previously, nanoscaled materials in different dimensional structures have been synthesised. However, few investigations have focused on the dimension-dependent effects [7,9]. In this study, several nanocarbons in different dimensions, such as 0D C_{60}, 1D single-wall carbon nanotubes (SWCNTs), 2D GNP, and 3D CMK-3 and CMK-8, were employed for adsorptive and catalytically oxidative removal of organic pollutants in water. In addition, thermal

* Corresponding authors. Tel.: +61 892663776; fax: +61 892662681.
E-mail addresses: h.sun@curtin.edu.au (H. Sun), shaobin.wang@curtin.edu.au
(S. Wang).

treatment at a low temperature of 350 °C in nitrogen was applied to tune the physicochemical properties of the nanocarbons. As a result, enhanced adsorption and catalysis in phenol removal on some nanocarbons were observed. The mechanism of the enhanced performances for removing organic pollutants in water was discussed.

2. Experimental

2.1. Materials and chemicals

Fullerene (C_{60}, >99.5%), graphene nanoplate (GNP, >99.5%, size of 1–5 μm, thickness of 1–5 nm, S_{BET} > 90 m^2/g), hexagonally-ordered mesoporous carbon (CMK-3, >99.6%, size of 1.0 μm, pore size of 3.8–4 nm, S_{BET} > 900 m^2/g) and cubically-ordered mesoporous carbon (CMK-8, >99.6%, size of 0.5 μm, pore size of 3.2 nm, S_{BET} > 720 m^2/g) were obtained from XF Nano (China), while single-walled carbon nanotubes (SWCNTs, >95.0%, 5–30 μm in length, outside diameter <2 nm, S_{BET} > 380 m^2/g) were received from Timesnano (China). The metal-free nature of the carbon materials was confirmed by the analysis of acidic digestion solutions of the nanocarbons using a Perkin-Elmer Optima 8300 ICP-OES. These materials were then annealed at 350 °C for 1 h in a tube furnace under nitrogen atmosphere. The thermally treated samples were denoted as nanocarbon (C_{60}, SWCNTs, GNP, CMK-3 or CMK-8)-T. Potassium peroxymonosulfate (Oxone®) was obtained from Sigma–Aldrich. Phenol and methanol were obtained from Chem-Supply, Australia.

2.2. Characterisation of nanocarbons

X-ray diffraction (XRD) patterns were acquired on a Bruker D8-Advanced X-ray instrument using Cu-Kα radiation with λ at 1.5418 Å. Nitrogen sorption isotherms were obtained on a Micrometrics Tristar 3000 and the Brunauer–Emmet–Teller (BET) and Barrett–Joyner–Halenda (BJH) methods were applied to evaluate the specific surface area (SSA) and pore size distribution, respectively, of the samples. Fourier transform infrared spectra (FTIR) were recorded on a Bruker instrument with an ATR correction mode. X-ray photoelectron spectroscopy (XPS) was used to determine the chemical states of elements using a Thermo Escalab 250 with Al-Kα X-ray. Thermogravimetric-differential scanning calorimetry (TG-DSC) was carried out in an air flow at a flowrate of 100 mL/min using a PerkinElmer Diamond thermal analyser. Scanning electron microscopy (SEM) was applied to investigate the morphology of the carbons on Zeiss Neon 40 EsB FIBSEM. Raman analysis was performed on an ISA dispersive Raman spectroscopy using argon ion laser with a wavelength at 514 nm. The points of zero charge (PZC) of the carbon samples were measured using a Malvern Zetasizer Nano ZS.

2.3. Adsorption and catalytic oxidation of aqueous phenol solutions

The kinetic study of phenol adsorption was carried out in a 500 mL conical flask with phenol solution (20 ppm) and carbon adsorbents (0.2 g/L) in a temperature-controlled water bath keeping the temperature at 25 °C. The catalytic oxidation of phenol was carried out in the same condition with addition of PMS (2.0 g/L). During each time interval, 1 mL solution was withdrawn by a syringe, filtered by a 0.45 μm Millipore film, and injected into a vial. Then 0.5 mL of methanol was injected into the reaction solution as a quenching reagent to immediately stop further oxidation in the vial. The mixed solution was analysed by a high performance liquid chromatography (HPLC, Varian) with a C-18 column and a UV detector set at 270 nm. The initial solution pH was 6.5–7.0, and

during the catalytic oxidation, the solution pH had been almost constant at 2.5–3.0. Electron paramagnetic resonance (EPR) spectroscopy (Bruker EMX-E spectrometer, Germany) was applied for in situ investigation of the generation of reactive radicals, using 5, 5-dimethyl-pyrroline-oxide (DMPO) as the spin trapping reagent.

3. Results and discussion

3.1. Characterisation of carbon samples

XRD technique was applied to investigate the crystal structures and the potential effects of thermal treatment on various dimensional nanocarbons. Fig. 1(a) shows XRD patterns of 0D nanocarbons of C_{60} and C_{60}-T. Several strong peaks were observed on C_{60}, and the peaks at 10.9, 17.8, 20.9, 21.0, 27.5, 28.2, 31.0 and 32.9° are corresponding to specific (hkl) planes of (0 0 2), (1 1 0), (1 1 2), (0 0 4), (2 1 0), (1 1 4), (3 0 0) and (0 0 6), respectively [23]. It is noted that the absence of the strong (1 0 1) diffraction peak suggested that the order of hexagonal close-packed structure was not perfect. Compared to the pristine C_{60}, no obvious changes in XRD pattern were observed after annealing at 350 °C for 1 h under nitrogen atmosphere.

Fig. 1(b) shows XRD patterns of 1D SWCNTs and SWCNTs-T. Two characteristic peaks were found approximately at $2\theta = 26°$ and 43°, corresponding to (0 0 2) and (1 0 0) planes, respectively [24,25]. XRD characteristic peaks of GNP were consistent well with those of graphene. The 2θ peak can be observed at approximate 26.5° corresponding to (0 0 2) plane of graphite with d spacing of 0.34 nm. For CMK-3 and CMK-8, XRD patterns (Fig. 1(c)) showed a very weak signal at about $2\theta = 23°$. As seen, there were no additional peaks of other crystalline structures (guest species) for all the carbon nanomaterials, indicating the high purity of these carbons. Half peak width (B) and interlayer thickness (L) of nanocarbons and nanocarbon-Ts are listed in Table 1. Generally, thermal annealing at 350 °C did not impose significant effects on crystalline structures of the carbon materials.

Fig. S1 shows the Raman spectra of different carbon nanomaterials before and after thermal treatments. The D band and G band of these different carbon nanomaterials before the thermal annealing are consistent with previous studies [24,26–28]. The I_D/I_G ratios of different carbon nanomaterials are listed in Table 1. As seen, I_D/I_G ratio of CMK-8 slightly increased after thermal treatment. On the other hand, the I_D/I_G ratios of SWCNTs, GNP and CMK-3 slightly decreased. There was no significant effect of thermal annealing on the defective structures as indicated by the I_D/I_G ratios. The morphologies of different carbon nanomaterials are shown in SEM images (Fig. S2). Thermal treatments in this study would not result in significant changes in the morphology.

Fig. 2 shows pore size distributions and nitrogen sorption isotherms of the nanocarbons. 1D SWCNTs and 2D GNP showed good nitrogen adsorption, and 3D mesoporous carbons of CMK-3 and CMK-8 demonstrated much higher nitrogen adsorption volumes. Hysteresis loops between P/P_0 at 0.5–0.9 were observed on all the samples, indicating mesoporous structures of the nanocarbons. The specific surface areas (SSAs) of C_{60}, SWCNTs, GNP, CMK-3 and CMK-8 were estimated to be 5.0, 366, 103, 1129, and 1040 m^2/g, respectively. After thermal treatment at 350 °C for 1 h, nitrogen adsorption was generally enhanced on the samples and the SSAs were increased to 6.0, 442, 129, 1246 and 1167 m^2/g, accordingly. The SSA of SWCNTs (366 m^2/g) was in good agreement with the as-received value (380 m^2/g) [29,30]. For CMK-3 and CMK-8, the SSA values were slightly higher than the data provided by the supplier [24,31,32].

The non-microporous surface areas were determined using the t-plot method. Fig. S3 shows the comparison of total surface area
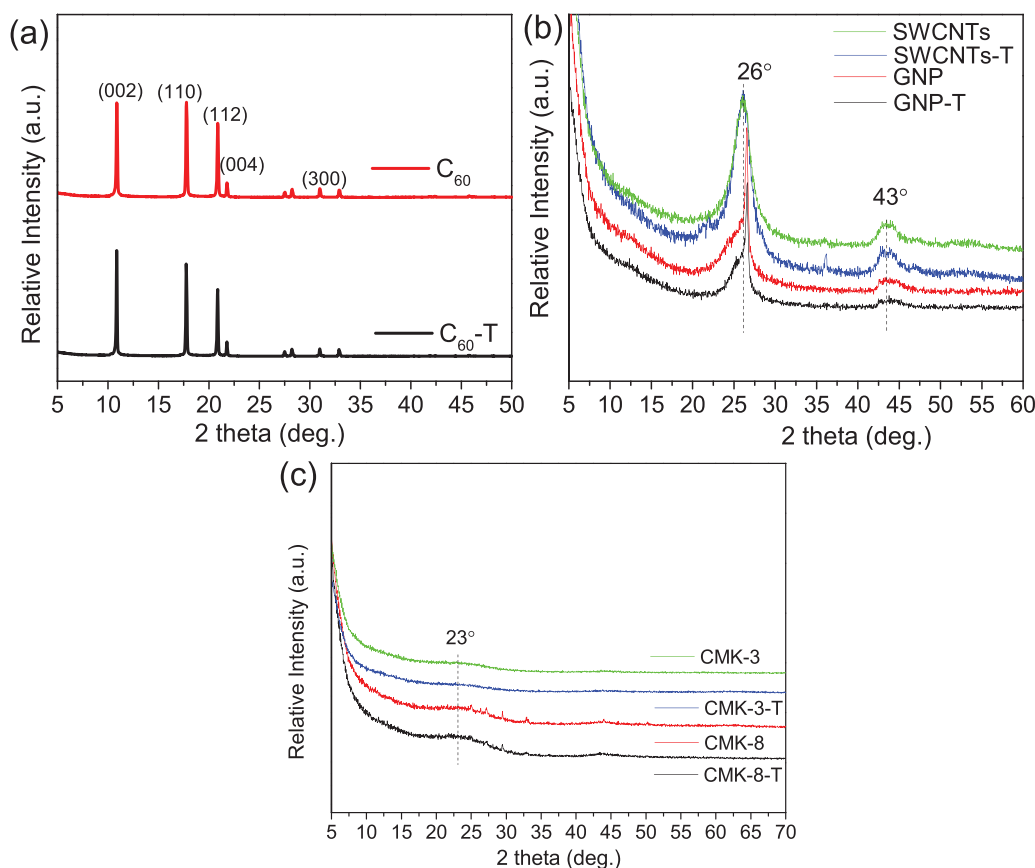
Fig. 1. XRD patterns of (a) C_{60} and C_{60}-T, (b) SWCNTs, SWCNTs-T, GNP, and GNP-T, (c) CMK-3, CMK-3-T, CMK-8, and CMK-8-T.

Table 1
Crystal- and micro-structures of different carbon nanomaterials.

Sample	Half peak width (B, °)	Interlayer material thickness (L, nm)	D band (cm^{-1})	G band (cm^{-1})	I_D/I_G ratio	SSA (m^2/g)	Pore size (nm)
C_{60}	–	–	–	–	–	5.0	5.9
C_{60}-T	–	–	–	–	–	6.0	5.3
SWCNTs	3.1	5.9	1332	1615	0.46	366	8.7
SWCNTs-T	2.9	6.3	1311	1572	0.43	442	8.8
GNP	1.0	18.2	1320	1569	1.28	103	13.5
GNP-T	0.7	25.9	1320	1569	1.27	129	14.5
CMK-3			1311	1583	1.17	1129	4.1
CMK-3-T	–	–	1311	1575	1.15	1246	4.1
CMK-8	–	–	1308	1577	1.49	1040	5.6
CMK-8-T	–	–	1308	1575	1.55	1167	5.9

(SSA) with microporous surface area and non-microporous surface area. Non-microporous area of C_{60}, SWCNT, GNP, CMK-3 and CMK-8 were 5, 352, 91, 1086 and 977 m^2/g, respectively. After thermal treatment, the non- microporous areas were increased to 6, 408, 126, 1131 and 993 m^2/g, accordingly. From these results, the mesopore contents of C_{60}, SWCNT, GNP, CMK-3 and CMK-8 were estimated to be 100, 96, 89, 96 and 94%, respectively, of the total surface area (SSA); and 100, 92, 98, 91, and 85% were determined for the carbon materials after thermal treatment.

The functional groups of the carbon materials were investigated by FTIR (Fig. 3). Two modes of T_{1u} (3) at 1181 cm^{-1} and T_{1u} (4) at 1427 cm^{-1} can be observed on C_{60} [33,34], corresponding to the tangential motion of the carbon atoms. It was also observed that fullerene has a stable carbon structure [35,36]. For SWCNTs, three main groups such as O—H group (hydroxyl) at 3336 cm^{-1}, C—H group (methyl) at 2911 cm^{-1}, and C=C group at 1575 cm^{-1} were appearing [37,38]. However, the C—H and O—H groups were absent after thermal annealing, which indicated the lack of hydrogen and oxygen groups due to thermal desorption. On the other hand, the aromatic group (C=C) at 1565 cm^{-1} remained with a decreased intensity. Only C=C group at 1555 cm^{-1} can be observed on GNP, which was slightly shifted to 1562 cm^{-1} after thermal treatment. That suggested a very low oxygen content on GNP. A few carbon groups, such as C—H groups at 2880 cm^{-1}, C=O group at 1700 cm^{-1}, C=C group at 1573 cm^{-1}, C—O group at 1428 cm^{-1} and 1135 cm^{-1} can be observed on CMK-3 [39]. After thermal treatment, the C=C group at 1562 cm^{-1} remained strong and other peaks became pale, due to the removal of hydrogen and oxygen groups [40,41]. Meanwhile, C=C group at 1559 cm^{-1} and C—O group at 1052 cm^{-1} can be seen on CMK-8, which showed slight changes to 1560 cm^{-1} and 1055 cm^{-1} after annealing. Fig. S4 shows the thermal analysis results of the nanocarbon samples. It can be found that before 400 °C, all the raw carbon materials are stable in air. Therefore, thermal treatment at 350 °C in nitrogen would only modulate the functional groups without any significant combustion or decomposition.
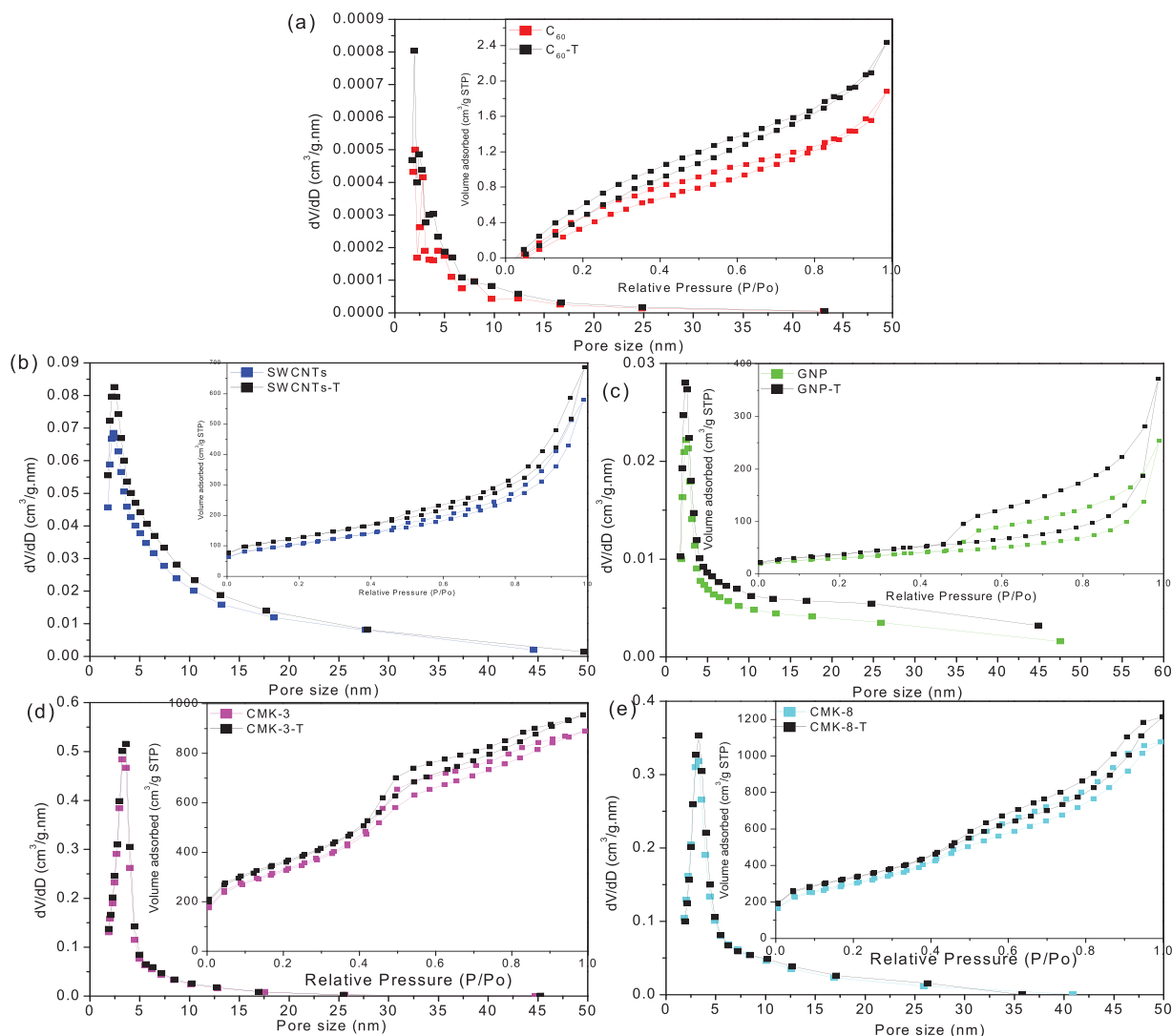
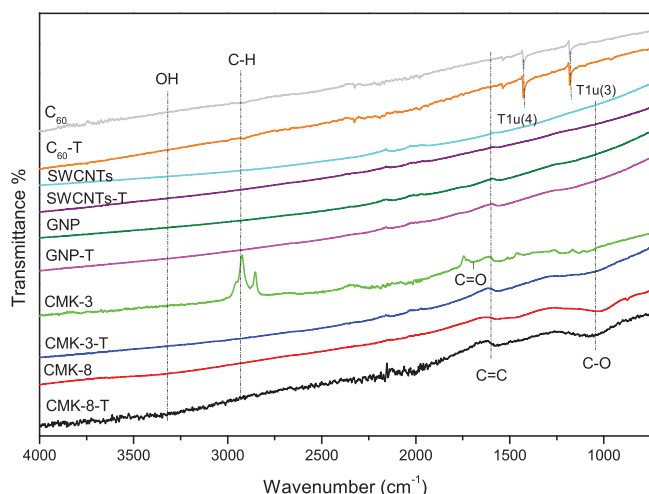**Fig. 2.** Pore size distributions of various nanocarbons. Insets: nitrogen sorption isotherms.

Fig. 3. FTIR spectra of different nanocarbons before and after thermal treatment in nitrogen.

Table 2
Chemical compositions of different nanocarbons before and after oxidation reactions.

Sample	O level, at.%	O/C ratio	O_1, at.%,	O_2, at.%,	O_3, at.%,
C_{60}	9.46	0.104	6.27	3.19	–
C_{60}-T	1.70	0.017	0.68	1.02	–
SWCNT	4.27	0.045	0.46	3.81	–
SWCNT-T	1.45	0.015	0.73	0.72	–
GNP	9.02	0.101	2.73	3.91	2.38
GNP-T	4.00	0.044	0.17	3.88	–
CMK-3	10.1	0.112	3.72	4.65	1.73
CMK-3-T	1.42	0.014	0.05	1.37	–
CMK-8	6.10	0.065	0.35	4.96	0.79
CMK-8-T	5.00	0.053	1.18	2.83	0.99
Used SWCNT (2nd run)	2.3	0.024	0.43	1.87	–
Used SWCNT (3rd run)	6.72	0.072	1.39	5.33	–
Used CMK-8 (2nd run)	12	0.14	1.28	6.91	3.82
Used CMK-8 (3rd run)	13.14	0.15	2.78	6.06	4.3

different carbon nanomaterials before and after thermal treatment were tabulated in Table 2. The changes in oxygen contents would adjust the surface features of the nanocarbons and therefore influence the adsorption and catalytic behaviour.

Figs. 4(b)–(f) show high resolution XPS O 1s spectra of different carbon nanomaterials. Two types of oxygen species can be seen from the de-convolution of XPS O 1s spectra in C_{60},
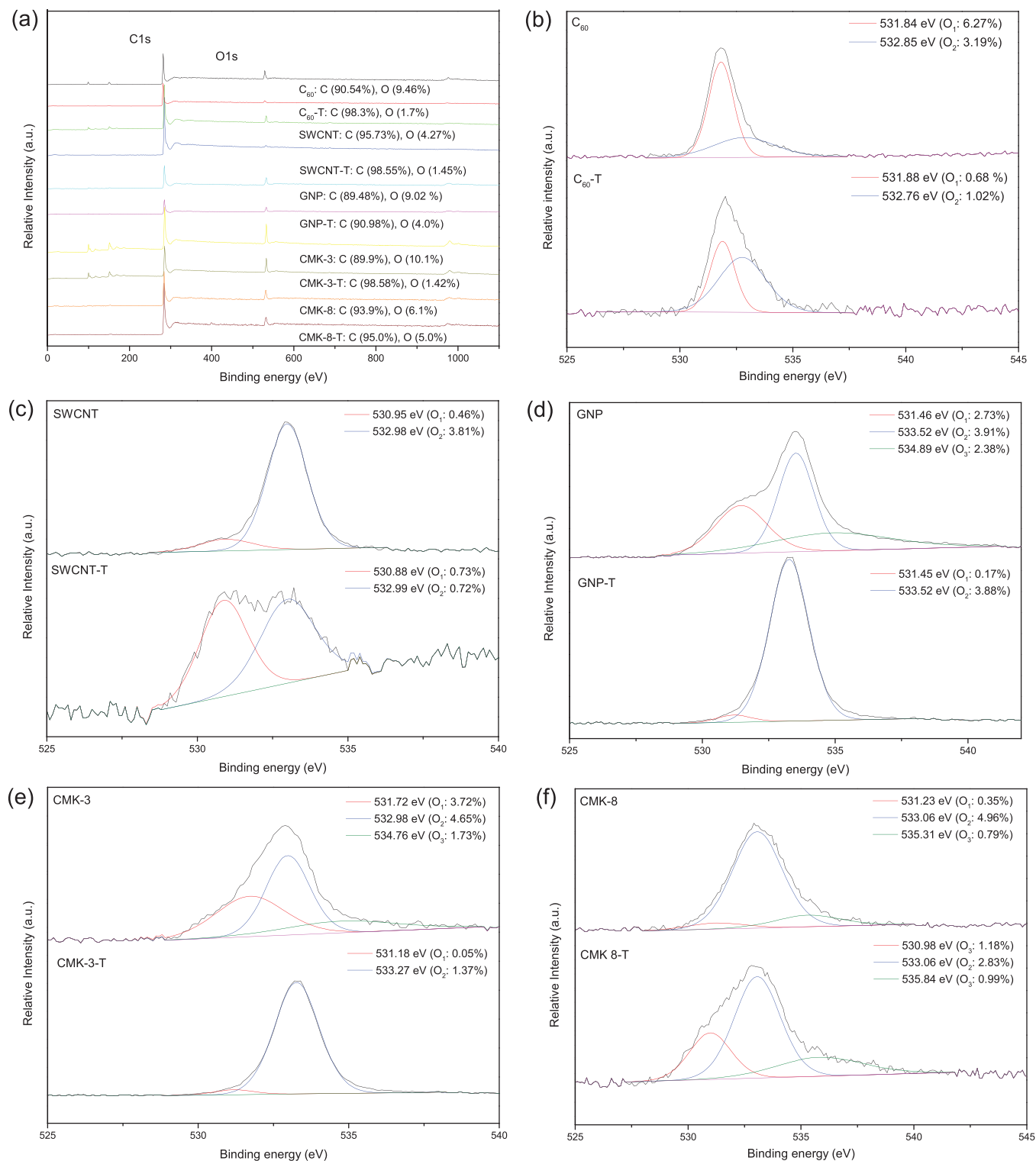
Fig. 4 shows XPS studies of different carbon nanomaterials. Fig. 4(a) shows that C 1s and O 1s peaks are centred at 284.7 and 532.2 eV, respectively [42–44]. The changes in oxygen contents for

Fig. 4. (a) XPS survey; O1s of (b) C_{60} and C_{60}-T, (c) SWCNT and SWCNT-T, (d) GNP and GNP-T, (e) CMK-3 and CMK-3-T, and (f) CMK-8 and CMK-8-T.

C_{60}-T, SWCNT, SWCNT-T, GNP-T and CMK-3-T: O_1 ($C=O$) at 530.84–531.88 eV and O_2 ($C-O-C$) at 532.76–533.0 eV [42]. Three types of oxygen species can be seen from the de-convolution of XPS O 1s spectra in GNP, CMK-3, CMK-8 and CMK-8-T: O_1 ($C=O$) at 530.98–531.8 eV, O_2 ($C-O-C$) at 532.9–533.6 eV, and O_3 (chemisorbed oxygen and adsorbed water) at 534.7–535.84 eV [39,43–45]. The O/C (oxygen versus carbon) ratios and levels of different oxygen-containing groups are listed in Table 2. The overall

oxygen contents were decreased after thermal treatment in nitrogen. For the specific oxygen groups, such as $C=O$, $C-O-C$, and chemisorbed groups/water showed different trends after thermal treatment. And the oxygen levels of specific groups (such as $C=O$ or chemisorbed groups/water) might increase due to the transformation of $C-O-C/C-O-H$. The changes of the contents of specific groups may also affect the catalytic performances of the carbon materials.
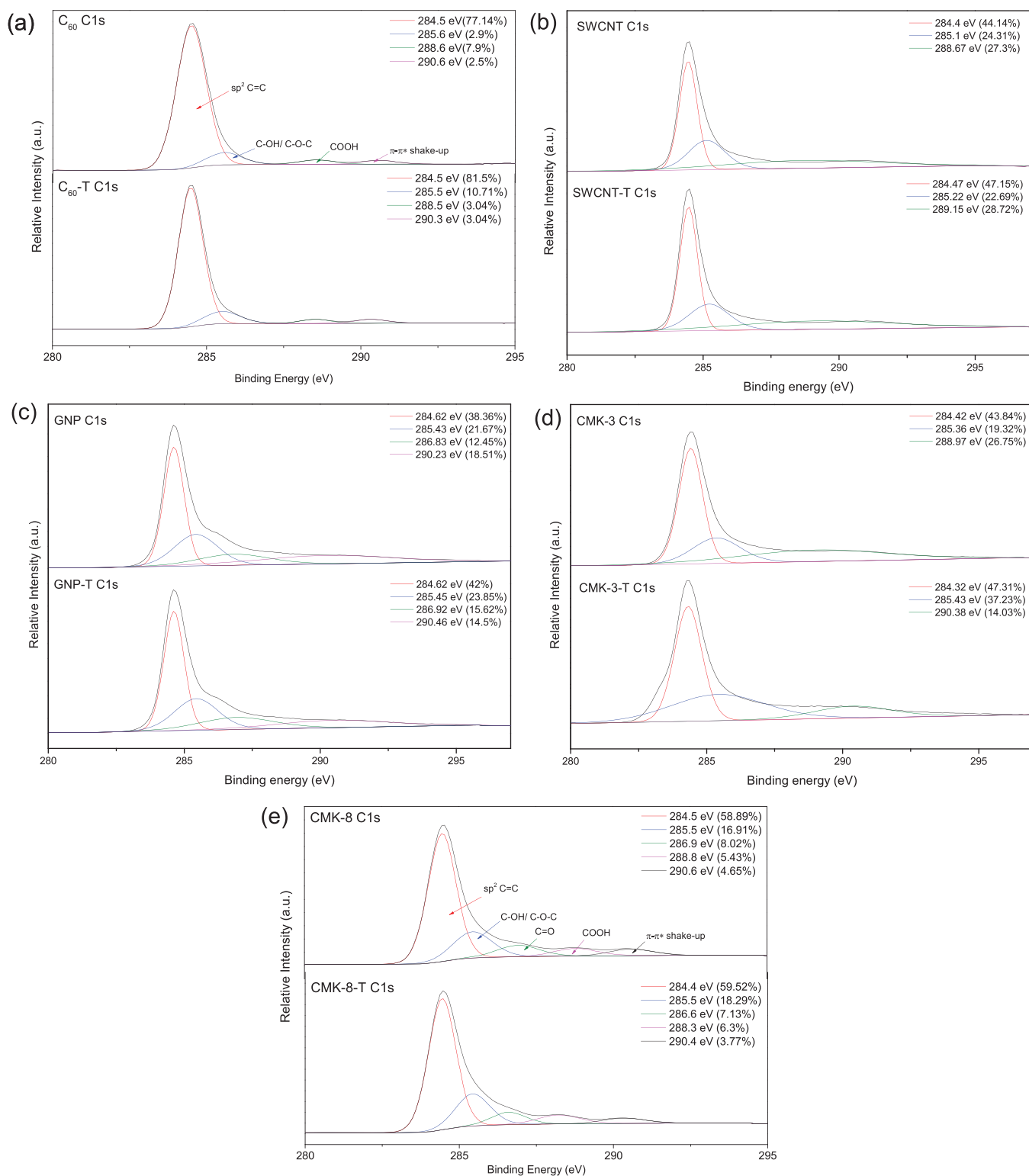
Fig. 5. (a) XPS C1s spectra of (a) C_{60} and C_{60}-T (b) SWCNT and SWCNT-T, (c) GNP and GNP-T, (d) CMK-3 and CMK-3-T, and (e) CMK-8 and CMK-8-T.

Fig. 5 shows the de-convolution XPS C1s spectra of different carbon nanomaterials. A broad C1s peak can be divided into four sections indicating four different C species for C_{60} and C_{60}-T in the range of 284–291 eV. For C_{60} and C_{60}-T, C=C, C—O—C/ C—O—H, COOH bond and $\pi-\pi^*$ shake up occurred at 284.5, 285.5, 288.5 and 290.3 eV, respectively [43,44]. A broad C1s peak indicated three different C species on SWCNT and SWCNT-T in the range of 284–289 eV: C=C, C—O—C, and COOH bond occurred at 284.5,

285.1 and 288.7 eV, respectively. A broad C1s peak indicated four different C species for GNP and GNP-T in the range of 284–291 eV: C=C, C—O—C, C=O and $\pi-\pi^*$ shake up bond occurred at 284.6, 285.4, 286.8 and 290.2 eV, respectively. A broad C1s peak indicated three different C species for CMK-3 and CMK-3-T in the range of 284–291 eV: C=C, C—O—C and $\pi-\pi^*$ shake up occurred at 284.3, 285.3 and 289 eV, respectively. A broad C1s peak indicated five different C species for CMK-8 and CMK-8-T in the range
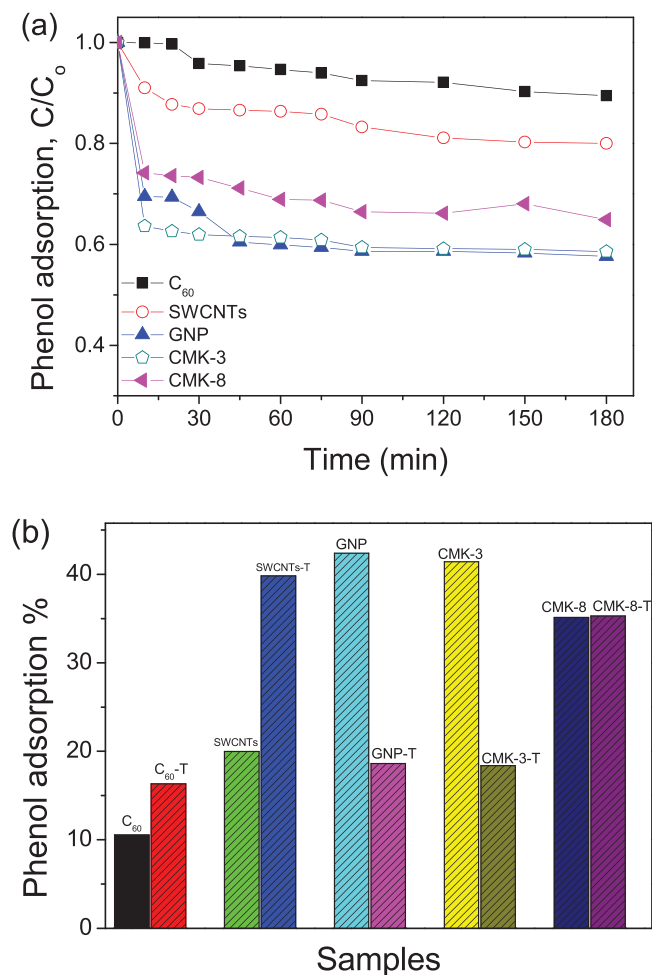
Fig. 6. (a) Adsorption of phenol on different pristine carbon nanomaterials, and (b) effect of thermal treatment in nitrogen on phenol adsorption in 180 min.

of 284–291 eV. For CMK-8 and CMK-8-T, C=C, C—O—C, C=O, COOH bond and π—π^* shake up occurred at 284.5, 285.5, 286.6, 288.3, and 290.4 eV, respectively [39,45]. The results confirmed the different oxygen functional groups on the surfaces of the nanocarbons.

3.2. Adsorption performance of nanocarbons

Fig. 6(a) shows dynamic phenol adsorption profiles on different unmodified carbons. All carbons exhibited fast adsorption and reached equilibrium quickly in 40 min. In 180 min, around 10% phenol was removed by C_{60}. Ballesteros et al. [46] also observed the poor adsorption of phenol on fullerene, which was attributed to the inferior interactions of C_{60} and polar functional groups of phenol. SWCNTs had a better adsorptive performance than C_{60}, providing around 20% phenol adsorption in 180 min. It was reported that carbon nanotubes are made of cylindrical graphitic sheets, which are of super hydrophobicity and very large van der Waals index, and that they have sp^2-hybridized carbon atoms with high electronic polarizability showing significant interaction with aromatic compounds via π-π coupling/stacking [47]. GNP had a lower SSA than SWCNTs, while it showed a much better adsorption at around 40% phenol removal in 180 min. The phenol adsorption of GNP was much higher than reported rGO samples [11,22]. The π–π bonds and flat structure of graphene might significantly contribute to the better adsorptive performance of GNP [13]. For the two mesoporous carbons, CMK-3 showed comparable adsorption to GNP, and higher

than CMK-8. The better adsorption was attributed to their much higher SSAs.

The effect of thermal treatment on phenol adsorption is shown in Fig. 6(b), in which phenol adsorption at 180 min on the materials before and after thermal treatment was compared. Enhanced adsorption was observed for C_{60} and SWCNTs after thermal treatment and phenol removal was increased from 10.5% and 20% to 16.3% and 39.8%, respectively. Significant decline in phenol adsorption was observed on GNP and CMK-3 after thermal treatment, which showed decreased phenol removal from 42.4% and 41.4% to 18.6% and 18.4%, respectively. On the other hand, adsorption of CMK-8 was remained almost unchanged after thermal treatment. Thermal treatment in nitrogen slightly increased SSA and removed the surface oxygen groups. The varied effect of thermal treatment on adsorption was due to the different adsorption mechanisms on different carbon materials.

Phenol adsorption on carbon materials has been generally classified as physisorption and chemisorption [48]. Physisorption of phenol depends strictly on the porosity (surface geometrical heterogeneity), whereas chemisorption depends on the availability of the basal planes (surface chemical heterogeneity). The presence of surface oxygen sites on carbon surface was suggested to have a capacity of chemisorption for binding phenol [49]. Three possible interactions between phenol and carbon surfaces were proposed: (a) a donor-acceptor complex interaction between the negatively charged aromatic ring of phenol and the positively charged basal plane of carbon containing oxygen functional groups [50], (b) a dispersive interaction between the phenol aromatic rings and the π-electrons of the graphitic carbon basal planes [51] and, (c) an electrostatic attraction and repulsion when ions are present [52]. In general, the practical phenol adsorption on the nanocarbons was a result of combined interactions as indicated above.

For pristine nanomaterials in this study, the adsorption performance at 180 min shows GNP (2D with SSA of 103 m^2/g) $\sim$ CMK-3 (3D with SSA of 1129 m^2/g) > CMK-8 (3D with SSA of 1040 m^2/g) > SWCNTs (1D with SSA of 366 m^2/g) > C_{60} (0D with SSA of 5 m^2/g). After thermal annealing at 350 °C, the adsorption performance at 180 min shows SWCNTs-T (1D with SSA of 442 m^2/g) > CMK-8-T (3D with SSA of 1167 m^2/g) > GNP-T (2D with SSA of 129 m^2/g) $\sim$ CMK-3-T (3D with SSA of 1246 m^2/g) > C_{60}-T (0D with SSA of 6 m^2/g). It appeared that phenol adsorption and dimensional structure of carbons are not in the same order. However, 2D and 3D nanocarbons show higher adsorption than 1D and 0D nanocarbons due to more porous structure for physisorption and the presence of edge defects with certain oxygen functional groups for chemisorption. After thermal treatment with removal of oxygen functional groups, phenol adsorption will be affected depending on structural dimension. Phenol adsorption will be enhanced on 0D and 1D, while phenol adsorption will be reduced for 2D and 3D nanocarbons. This suggests that phenol adsorption via sp^2 hybridized structure with porosity will play a significant role to enhance physisorption and that oxygen functional groups on the nanocarbon edge defects will influence carbon surface polarity to interact with phenol for chemisorption process. In this study, the chemisorption process for phenol adsorption may be due to the donor-acceptor complex interaction and the dispersive interaction without any preference.

C_{60} and C_{60}-T showed low adsorption capacity of phenol, which might be due to the low SSA for physisorption with very little contribution of chemisorption because of the minor edge defects. The improvement of phenol adsorption after thermal annealing was mainly due to the increased SSA. SWCNT and SWCNT-T show better phenol adsorption compared to C_{60} and C_{60}-T, due to the increase of SSA value and increase of mesopore content for physisorption with porosity pore size (8.7–8.8 nm) along with the moderate contribution of chemisorption because of edge defects (I_D/I_G = 0.46 and 0.43)

with certain oxygen functional groups. After thermal annealing and the decomposition of certain oxygen functional groups, SWCNT-T showed an increase of phenol adsorption owing to the enhanced physisorption. GNP showed the best phenol adsorption, which was mainly due to the dominant chemisorption because of the presence of edge defects (I_D/I_G = 1.28) with certain oxygen functional groups along with the moderate physisorption (SSA = 103 m^2/g) by porosity of pore size 13.5 nm. After thermal annealing, the phenol adsorption on GNP-T decreased significantly due to the lowered chemisorption because of the decomposition of certain oxygen functional groups. CMK-3 showed the second best phenol adsorption that might be due to the significant chemisorption from the presence of edge defects (I_D/I_G = 1.17) with certain oxygen functional groups. After thermal annealing, the phenol adsorption of CMK-3-T significantly decreased due to the decomposition of certain oxygen functional groups. CMK-8 showed the third best phenol adsorption. After thermal annealing, CMK-8-T showed almost similar phenol adsorption because the insignificant decrease of oxygen concentrations from 6.1% to 5% for chemisorption was compensated by the increase of SSA value from 1040 to 1167 m^2/g for physisorption.

Phenols have weak acidic properties and are preferable to be adsorbed on the basic surface. Some of the oxygen groups, such as carbonyl, carboxyl, phenolic hydroxyl and lactonic are acidic, while some groups, for example, pyrone, chromene and quinone are basic [48,49]. The points of zero charge of the carbon materials were evaluated to investigate the surface charges. The PZCs of C_{60} (C_{60}-T), GNP (GNP-T), SWCNT (SWCNT-T), CMK-3 (CMK-3-T), and CMK-8 (CMK-8-T) were determined to be 5.06 (5.33), 2.21 (2.41), 4.97 (4.29), 5.33 (5.10), and 4.08 (3.92), respectively. There was no direct correlation between PZCs and phenol adsorption that can be made for the pristine carbon materials. However, the changes of increased or decreased phenol adsorption after thermal treatments were consistent to the increased or decreased PZCs. The PZC changes were ascribed to the decomposition and evolution of oxygen groups before and after thermal treatment. Therefore, the almost unchanged phenol adsorption on CMK-8 and CMK-8-T could be explained by the minor effect on oxygen levels by the thermal treatment.

3.3. Catalytic oxidation of phenol

Fig. 7(a) shows the catalytic oxidation of phenol on different carbons by activation of PMS. For C_{60}, 15% phenol removal was rapidly achieved in 5 min, and then further 7% phenol removal occurred very slowly in 240 min. The phenol removal profile indicated an adsorption characteristic rather than effective catalysis. Continuous and effective phenol degradation was observed on SWCNTs, and around 100% phenol removal was achieved in 90 min. The efficient PMS activation on multi-walled carbon nanotubes was reported recently, showing around 65% phenol removal in 90 min [21], and a lower activity than SWCNTs in this study. On GNP, continuous phenol degradation was found in first 120 min providing around 50% phenol removal, and then the removal curve became flat. As GNP showed around 40% phenol removal in adsorption tests, the catalysis on GNP was not effective. The catalysis on GNP was not as good as rGO [4,11,20,22], which might be due to the different functional groups and defective structures. For the first time, this study observed the effective catalytic activation of PMS on CMK-3 and CMK-8. Complete phenol removal was achieved in 40 min on 3D hexagonally-ordered mesoporous carbon (CMK-3), while the reaction time for complete phenol decomposition was 210 min on cubically ordered mesoporous carbon (CMK-8). It has been reported that an activated carbon shows a similar activity [53].

A first-order kinetics was used to evaluate the rate constants in phenol degradation on the carbons. Fig. 7(b) shows the rate con-
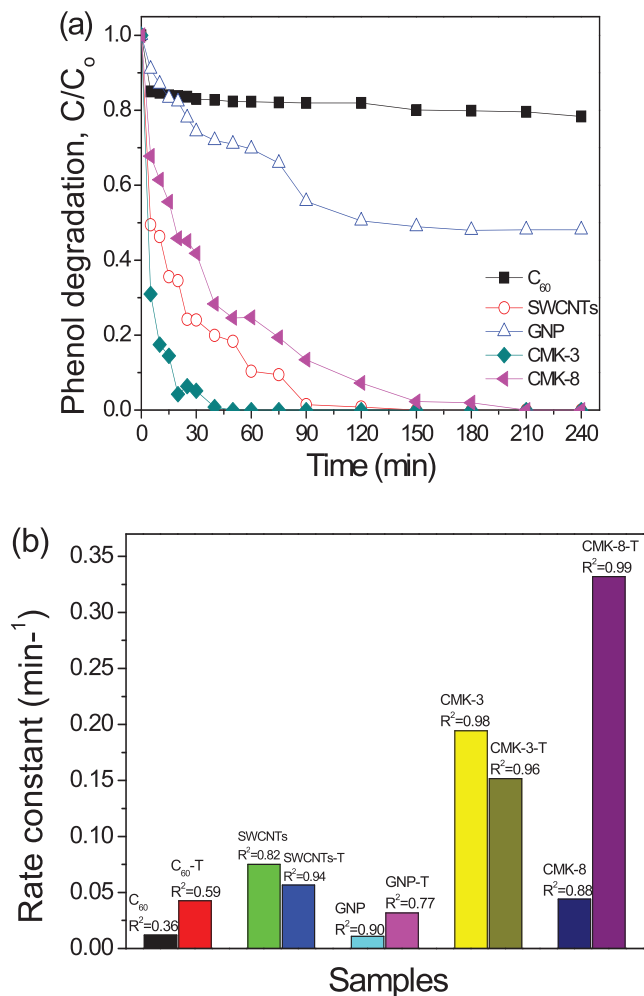

Fig. 7. (a) Catalytic degradation of phenol on pristine carbons, and (b) rate constants of phenol degradation on carbons before and after thermal treatment.

stants before and after thermal treatments. For pristine samples, the rate constants followed an order of CMK-3 > SWCNTs > CMK-8 > C_{60} ~ GNP. A varied effect of thermal treatment on catalysis of nanocarbons was also observed. Significant enhanced catalysis was achieved on C_{60}-T, GNP-T and CMK-8-T, but decreased catalysis was found on SWCNTs-T and CMK-3-T. It was very interesting to find that a 7.5-fold enhancement was found on CMK-8 after thermal treatment. As indicated before, the adsorption and SSA were not changed much after thermal treatment. XPS suggested that C=O groups was increased from 0.35 at.% to 1.18 at.%. In previous studies [11,20,22], the C=O was proposed to be one of the active sites for PMS activation. Yet such a case was not applied to C_{60}, due to the much high oxygen species, which is similar to GO [11]. However, a decrease in C=O groups was observed on CMK-3 and CMK-3-T from 3.72 at.% to 0.05 at.%. This was one of the reasons for the decreased phenol degradation on CMK-3 after thermal treatment, apart from the significant drop of adsorption ability.

In general, thermal annealing at 350 °C has the effect of the restoration of the pristine nanocarbon surfaces through the elimination of oxygen functional groups, increasing SSA values [4,13,20] and improving the performance of phenol degradation of 0D fullerene (C_{60}), and 1D SWCNTs. The catalytic phenol removal at 60 min for the 0D (C_{60}) increased from 17% to 52% after thermal annealing. This might be due to the restoration of C_{60} structure which resulted in a lower oxygen content and a higher conductivity [54]. For 1D SWCNTs and SWCNTs-T, the phenol removals by
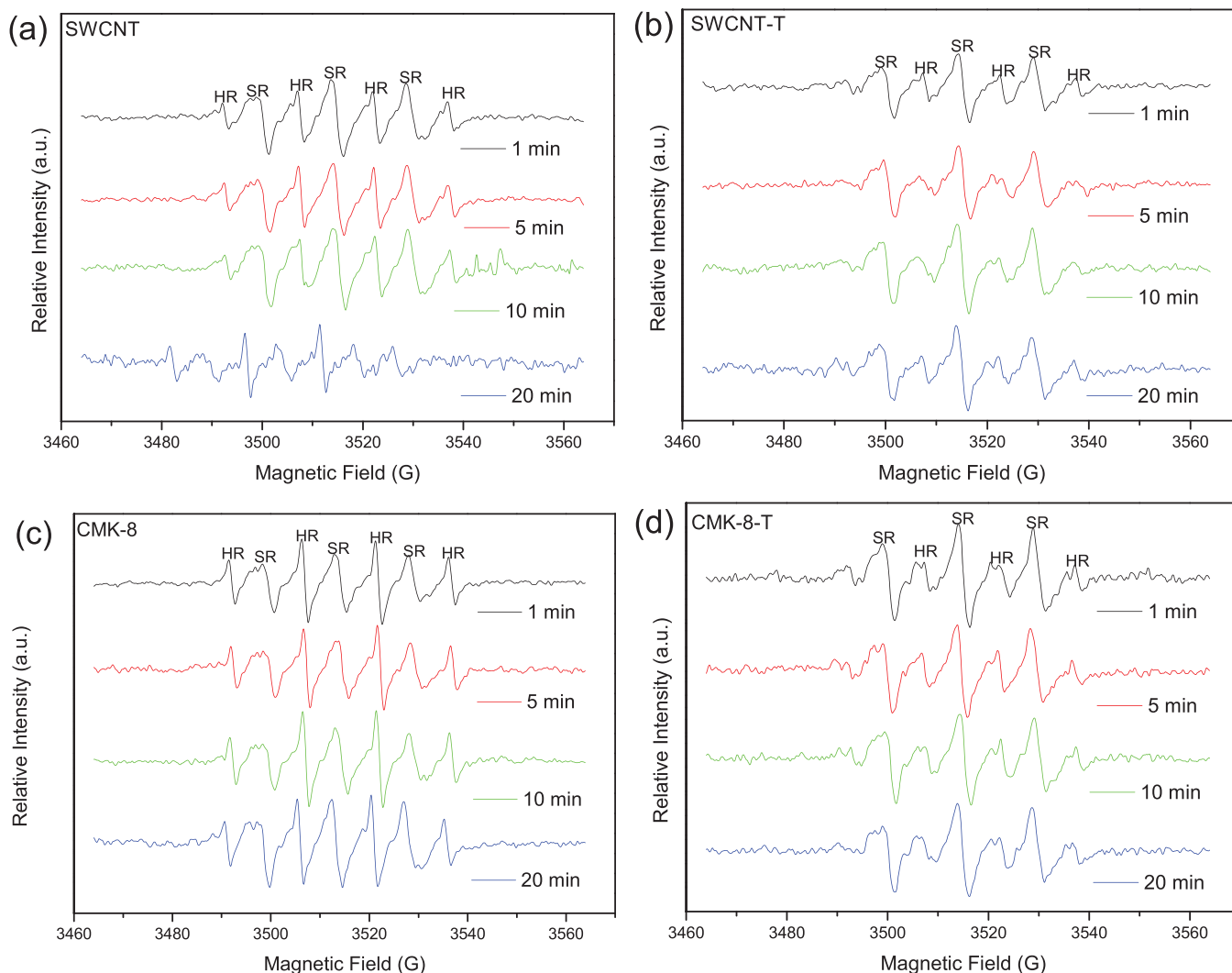
Fig. 8. EPR spectra of time-dependent generation and evolution of reactive radicals on (a) SWCNT, (b) SWCNT-T, (c) CMK-8, and (d) CMK-8-T. HR: hydroxyl radicals; SR: sulfate radicals.

catalytic oxidation at 60 min were 90% and 97%, respectively. In comparison with C_{60}, the better performance of 1D SWCNTs can be attributed to the presence of edge defects (zigzag or armchair) as indicated by the I_D/I_G ratios (0.46-0.43) and the contribution of rather high SSAs (366 and 442 m²/g) [30,55]. For 2D GNP, phenol oxidation at 60 min increased from 30% to 62% after thermal annealing. This improvement might also be due to the restoration of GNP structure which led to a lower oxygen content and a higher conductivity, the presence of edge defects and a slight increase of SSA values from 103 to 128 m²/g [4,20]. In comparison with the 1D SWCNTs, a lower phenol catalytic oxidation can be ascribed to their lower SSA. For 3D CMK-3 and CMK-3-T, phenol removals by catalytic oxidation at 60 min were 100%. It was suggested that 3D hexagonally-ordered mesoporous structure has provided sufficient edged defects with the contribution of high SSA of 1129 m²/g even in the pristine condition [24,56]. For the 3D CMK-8 and CMK-8-T, catalytic oxidation of phenol at 60 min was 76% and 100%, respectively. The enhancement was possibly attributed to the restoration of CMK-8 surface resulting in a lower oxygen content and a higher conductivity (which increases the electron transfer between carbon and PMS for a fast activation), and the presence of edge defects [31,57].

Furthermore, first-order kinetics was used to evaluate the rate constants in phenol degradation on SWCNT and CMK-8. Fig. S5

shows the rate constants of phenol catalytic oxidation on SWCNT and CMK-8, with the initial phenol concentrations at 20, 30 and 50 ppm. The higher the initial phenol concentration, the lower the efficiency of the phenol degradation, as shown in Fig. 5(a) and (b). Fig. S5(c) and (d) show that the reaction rate constants decreased from 0.038 (20 ppm) to 0.0068 (30 ppm) and 0.0035 min⁻¹ (50 ppm) for SWCNT; and from 0.0213 (20 ppm) to 0.0115 (30 ppm) and 0.003 min⁻¹ (50 ppm) for CMK-8, respectively.

Total organic carbon (TOC) after catalytic phenol oxidation for 180 min on different nanocarbons was measured. In general, TOC removal was slower than phenol degradation. It was found that CMK-3 was able to reduce 50.5% of TOC. Other TOC removals were determined to be 18.1%, 19.5%, 3.8% and 26.7% on CMK-8, GNP, C_{60}, and SWCNT, respectively.

One of the metal-free nanocarbons, CMK-3-T, was employed to check the catalyst stability, as shown in Fig. S6. It was seen that in the second run, 80% phenol removal was achieved within 240 min. In the third run, CMK-3-T was no longer efficient in catalytic oxidation which only removed phenol about 20% in 240 min. The poor catalytic stability of nanocarbons still needs improvement in future studies [11,21,58].

Fig. S7 shows XPS analysis of the used catalysts. Fig. S7(b) and (c) present high resolution XPS O 1s spectra of used SWCNT and CMK-8. Two types of oxygen species can be seen from the de-
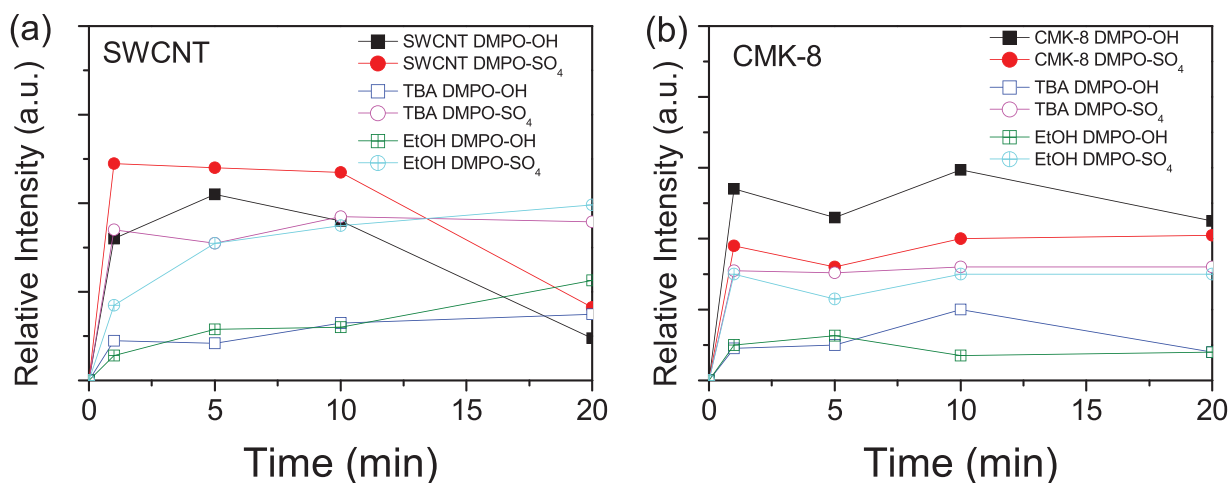
Fig. 9. Time-dependent evolutions of reactive radicals on (a) SWCNT and (b) CMK-8 with addition of quenching reagents. TAB: *tert*-butanol; EtOH: ethanol.

convolution of XPS O 1s spectra in the used SWCNT (2nd and 3rd run): O_1 (C=O) at 530.88 and 531.5 eV and O_2 (C—O—C) at 533.0 and 533.28 eV. Three types of oxygen species can be identified from the de-convolution of XPS O 1s spectra in the used CMK-8 (2nd and 3rd run): O_1 (C=O) at 531.43 and 531.72 eV, O_2 (C—O—C) at 533.06 and 533.25 eV, and O_3 (chemisorbed oxygen and adsorbed water) at 536 and 535.5 eV. The O/C (oxygen versus carbon) ratios and levels of different oxygen-containing groups are listed in Table 2. The overall oxygen content for SWCNT (4.27%) was decreased to 2.3% after undergoing 240 min oxidation reaction (2nd run) and was increased to 6.72% after the 3rd run. The overall oxygen contents for CMK-8 (6.1%) was increased to 12% after undergoing 240 min oxidation reaction (2nd run) and was increased to 13.14% after the 3rd run. Fig. S7(d) and (e) display the de-convolution XPS C1s spectra of used SWCNT and CMK-8. Changes related to oxygen functional groups were also observed.
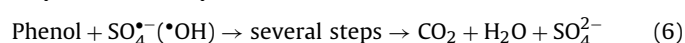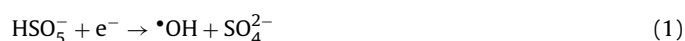
3.4. Mechanism of PMS activation and phenol oxidation

It was discovered that PMS can be activated by either metal-based or metal-free catalysts to generate both hydroxyl radicals (•OH) and sulfate radicals ($SO_4^{•-}$) [19,21]. Electron paramagnetic resonance (EPR) spectroscopy can be used to monitor the generation and evolution of the reactive radicals by catalytic activation of PMS [58–60]. In this study, the time-dependent evolutions of hydroxyl and sulfate radicals were monitored by EPR. The results obtained from the two efficient catalysts of SWCNT and CMK-8 and their derivatives were shown in Fig. 8. EPR spectra from other carbon materials can be found in Fig. S8. It can be seen that both hydroxyl radicals (•OH) and sulfate radicals ($SO_4^{•-}$) were present in the catalytic oxidation processes. Then the roles of the reactive radicals were further studied by competitive radical tests.

It was known that •OH and $SO_4^{•-}$ radicals show different reaction rates with two radical scavengers, ethanol (EtOH) and *tert*-butyl alcohol (TBA). The quenching agent of EtOH can capture both •OH and $SO_4^{•-}$ while TBA prefers capturing •OH radicals rather than $SO_4^{•-}$ radicals [58]. Fig. 9 displays the changes of reactive radicals generated by SWCNT and CMK-8 activation of PMS with different quenching reagents. Both radicals and their changes upon addition of classical quenching reagents were identified. The associated EPR spectra are shown in Fig. S9. Without the scavengers, the DMPO-OH intensities remained stable (SWCNT and CMK-8 DMPO–OH curves) within first 5 min and decreased afterwards. The DMPO–SO$_4$ intensities remained stable at a low level, which might be due to the great consumption of sulfate radicals in phenol oxidation. In the

presence of EtOH, DMPO–OH intensities reduced and the peak occurred at 5 min. Meanwhile, in the presence of TBA, DMPO–OH intensities were similar to that with the presence of EtOH. However, DMPO–SO$_4$ intensities did not show much difference with or without the scavengers. The above results suggest that both radicals are important for phenol degradation.

With the combination of EPR studies and classical quenching tests, •OH and $SO_4^{•-}$ radicals were confirmed to be present in PMS activation for phenol oxidation on different carbon nanomaterials. The electron transfer processes facilitated by carbon catalysis for phenol degradation can be described in below reactions [58].

$$HSO_5^- + e^- \rightarrow {}^{•}OH + SO_4^{2-} \tag{1}$$

$$HSO_5^- + e^- \rightarrow SO_4^{•-} + OH^- \tag{2}$$

$$HSO_5^- - e^- \rightarrow SO_5^{•-} + H^+ \tag{3}$$

$${}^{•}OH + SO_4^{2-} \rightarrow SO_4^{•-} + OH^- \tag{4}$$

$$SO_4^{•-} + OH^- \rightarrow SO_4^{2-} + {}^{•}OH \tag{5}$$

$$Phenol + SO_4^{•-}({}^{•}OH) \rightarrow several\ steps \rightarrow CO_2 + H_2O + SO_4^{2-} \tag{6}$$

The different phenol degradation efficiencies were suggested to be controlled by the above processes, which were indeed determined by the nature of the carbon catalysts, for example, the electron transfer rate, the selective production of the reactive radicals, and the ability for carrying out surface reactions.

4. Conclusions

In conclusion, properties of carbon nanomaterials in different structural dimensions (0–3D) before and after thermal annealing employing nitrogen gas at 350 °C were investigated and used for phenol adsorption and metal-free catalytic oxidation. The materials are C_{60}, SWCNTs (single wall carbon nanotubes), GNP (graphene nanoplate), CMK-3 and CMK-8 (ordered mesoporous carbon). Pristine nanocarbons showed varied phenol adsorption and the adsorptive performances followed the order of GNP ∼ CMK-3 > CMK-8 > SWCNTs > C_{60}, while the catalysis followed another order of CMK-3 > SWCNTs > CMK-8 > GNP > C_{60}. Thermal treatment at a lower temperature would not significantly change the SSA and crystal structure but could dramatically modify the surface functional groups. As a result, enhanced adsorption was found on SWCNTs by 2-fold and superior catalysis was achieved on CMK-8 by 7.5-fold after thermal treatment. Structural dimension can influence nanocarbon performance in adsorption and catalysis and surface oxygen functionality can also affect the adsorption

and catalysis. 0D C_{60} exhibited the lowest adsorption capacity and catalytic activity while 3D CMK-3 generally presented higher adsorption capacity and catalytic activity than 1D SWCNT and 2D GNP. The adsorption and catalysis were controlled by the integrated effects of structure, surface and chemical composition of the different nanocarbons.

Acknowledgements

Appendix A. Supplementary data

Supplementary data associated with this article can be found, in the online version, at http://dx.doi.org/10.1016/j.apcatb.2015.05.049

References

[1] H.W. Liang, Y.Y. Ting, H.Q. Sun, H.M. Ang, M.O. Tade, S.B. Wang, J. Colloid Interface Sci. 372 (2012) 58–62.
[2] G.M. Gadd, J. Chem. Technol. Biotechnol. 84 (2009) 13–28.
[3] P.R. Shukla, S.B. Wang, H.Q. Sun, H.M. Ang, M. Tade, Appl. Catal. B 100 (2010) 529–534.
[4] W.C. Peng, S.Z. Liu, H.Q. Sun, Y.J. Yao, L.J. Zhi, S.B. Wang, J. Mater. Chem. A 1 (2013) 5854–5859.
[5] C.D. Liang, Z.J. Li, S. Dai, Angew. Chem. Int. Ed. 47 (2008) 3696–3717.
[6] E. Haque, N.A. Khan, S.N. Talapaneni, A. Vinu, J. Jegal, S.H. Jhung, Bull. Korean Chem. Soc. 31 (2010) 1638–1642.
[7] E. Saputra, S. Muhammad, H.Q. Sun, H.M. Ang, M.O. Tade, S.B. Wang, Appl. Catal. B 154 (2014) 246–251.
[8] H.Q. Sun, G.L. Zhou, S.Z. Liu, H.M. Ang, M.O. Tade, S.B. Wang, Chem. Eng. J. 231 (2013) 18–25.
[9] E. Saputra, S. Muhammad, H.Q. Sun, H.M. Ang, M.O. Tade, S.B. Wang, Environ. Sci. Technol. 47 (2013) 5882–5887.
[10] G.L. Zhou, H.Y. Tian, H.Q. Sun, S.B. Wang, C.E. Buckley, Chem. Eng. J. 171 (2011) 1399–1405.
[11] H.Q. Sun, S.Z. Liu, G.L. Zhou, H.M. Ang, M.O. Tade, S.B. Wang, ACS Appl. Mater. Interfaces 4 (2012) 5466–5471.
[12] Y.X. Yang, K. Chiang, N. Burke, Catal. Today 178 (2011) 197–205.
[13] S.B. Wang, H.Q. Sun, H.M. Ang, M.O. Tade, Chem. Eng. J. 226 (2013) 336–347.
[14] E. Saputra, S. Muhammad, H.Q. Sun, H.M. Ang, M.O. Tade, S.B. Wang, Appl. Catal. B 142 (2013) 729–735.
[15] S.K. Ling, S.B. Wang, Y.L. Peng, J. Hazard. Mater. 178 (2010) 385–389.
[16] K.H. Chan, W. Chu, Water Res. 43 (2009) 2513–2521.
[17] Q.J. Yang, H. Choi, Y.J. Chen, D.D. Dionysiou, Appl. Catal. B 77 (2008) 300–307.
[18] G.P. Anipsitakis, D.D. Dionysiou, M.A. Gonzalez, Environ. Sci. Technol. 40 (2006) 1000–1007.
[19] G.P. Anipsitakis, D.D. Dionysiou, Environ. Sci. Technol. 37 (2003) 4790–4797.
[20] S.Z. Liu, W.C. Peng, H.Q. Sun, S.B. Wang, Nanoscale 6 (2014) 766–771.
[21] H.Q. Sun, C. Kwan, A. Suvorova, H.M. Ang, M.O. Tade, S.B. Wang, Appl. Catal. B 154 (2014) 134–141.
[22] H. Sun, Y. Wang, S. Liu, L. Ge, L. Wang, Z. Zhu, S. Wang, Chem. Commun. 49 (2013) 9914–9916.
[23] W. Kratschmer, L.D. Lamb, K. Fostiropoulos, D.R. Huffman, Nature 347 (1990) 354–358.
[24] S.D. Choi, J.H. Lee, D.M. Park, G.J. Kim, Bull. Korean Chem. Soc. 34 (2013) 2155–2161.
[25] Z. Wang, D.C. Ba, F. Liu, P.J. Cao, T.Z. Yang, Y.S. Gu, H.J. Gao, Vacuum 77 (2005) 139–144.
[26] C.C. Ciobotaru, C.M. Damian, H. Iovu, UPB Sci. Bull. Ser. B 75 (2013) 55–66.
[27] S.C. Lu, M.G. Yao, X.G. Yang, Q.J. Li, J.P. Xiao, Z. Yao, L.H. Jiang, R. Liu, B. Liu, S.L. Chen, B. Zou, T. Cui, B.B. Liu, Chem. Phys. Lett. 585 (2013) 101–106.
[28] M. Ignat, E. Popovici, Revue Roum. Chim. 56 (2011) 947–952.
[29] Y. Ye, C.C. Ahn, C. Witham, B. Fultz, J. Liu, A.G. Rinzler, D. Colbert, K.A. Smith, R.E. Smalley, Appl. Phys. Lett. 74 (1999) 2307–2309.
[30] S. Chakraborty, J. Chattopadhyay, H.Q. Peng, Z.Y. Chen, A. Mukherjee, R.S. Arvidson, R.H. Hauge, W.E. Billups, J. Phys. Chem. B 110 (2006) 24812–24815.
[31] M. Lezanska, J. Wloch, G. Szymanski, I. Szpakowska, J. Kornatowski, Catal. Today 150 (2010) 77–83.
[32] G. Zolfaghari, A. Esmaili-Sari, M. Anbia, H. Younesi, S. Amirmahmoodi, A. Ghafari-Nazari, J. Hazard. Mater. 192 (2011) 1046–1055.
[33] J. Rymarczyk, A. Kaminska, J. Keczkowska, M. Kozlowski, E. Czerwosz, Opt. Appl. 43 (2013) 123–132.
[34] T. Wadayama, T. Ohta, A. Hatta, Israel J. Chem. 46 (2006) 257–263.
[35] D.S. Bethune, G. Meijer, W.C. Tang, H.J. Rosen, W.G. Golden, H. Seki, C.A. Brown, M.S. Devries, Chem. Phys. Lett. 179 (1991) 181–186.
[36] S. Thomas, N. Kalarikkal, A.M. Stephan, B. Raneesh, Advanced Nanomaterials: Synthesis, Properties, and Applications, Apple Academic Press, 2014.
[37] H.M. Park, K.H. Kim, S.H. Lee, D.H. Park, Y.K. Hong, J. Joo, Colloids Surf. A 313 (2008) 72–76.
[38] R.A. Meyers, Encyclopedia of Analytical Chemistry, Wiley, 2012.
[39] D.S. Su, J.J. Delgado, X. Liu, D. Wang, R. Schlogl, L.F. Wang, Z. Zhang, Z.C. Shan, F.S. Xiao, Chem. Asian J. 4 (2009) 1108–1113.
[40] D.S. Yuan, J. Zeng, J. Chen, Y. Liu, Int. J. Electrochem. Sci. 4 (2009) 562–570.
[41] W.J. Zou, S.S. Mo, S.L. Zhou, T.X. Zhou, N.N. Xia, D.S. Yuan, J. Electrochem. Sci. Eng. (2011), http://dx.doi.org/10.5599/jese.2011.0001
[42] D. Briggs, Surface Analysis of Polymers by XPS and Static SIMS, Cambridge University Press, 1998.
[43] Y.M. Xie, P.M.A. Sherwood, Appl. Spectrosc. 43 (1989) 1153–1158.
[44] Y.M. Xie, P.M.A. Sherwood, Chem. Mater. 2 (1990) 293–299.
[45] H. Darmstadt, C. Roy, S. Kaliaguine, S.J. Choi, R. Ryoo, Carbon 40 (2002) 2673–2683.
[46] E. Ballesteros, M. Gallego, M. Valcarcel, J. Chromatogr. A 869 (2000) 101–110.
[47] L.L. Ji, Y. Shao, Z.Y. Xu, S.R. Zheng, D.Q. Zhu, Environ. Sci. Technol. 44 (2010) 6429–6436.
[48] L.F. Velasco, C.O. Ania, Adsorpt. J. Int. Adsorpt. Soc. 17 (2011) 247–254.
[49] A. Dabrowski, P. Podkoscielny, Z. Hubicki, M. Barczak, Chemosphere 58 (2005) 1049–1070.
[50] K. Laszlo, P. Podkoscielny, A. Dabrowski, Langmuir 19 (2003) 5287–5294.
[51] J.A. Mattson, H.B. Mark Jr., M.D. Malbin, W.J. Weber Jr., J.C. Crittenden, J. Colloid Interface Sci. 31 (1969) 116–130.
[52] R.W. Coughlin, F.S. Ezra, Environ. Sci. Technol. 2 (1968) 291–297.
[53] E. Saputra, S. Muhammad, H.Q. Sun, S.B. Wang, RSC Adv. 3 (2013) 21905–21910.
[54] C. Gomez-Navarro, M. Burghard, K. Kern, Nano Lett. 8 (2008) 2045–2049.
[55] S.M. Huang, X.Y. Cai, J. Liu, J. Am. Chem. Soc. 125 (2003) 5636–5637.
[56] A. Nsabimana, X.J. Bo, Y.F. Zhang, M. Li, C. Han, L.P. Guo, J. Colloid Interface Sci. 428 (2014) 133–140.
[57] T. Maiyalagan, A.A. Nassr, T.O. Alaje, M. Bron, K. Scott, J. Power Sources 211 (2012) 147–153.
[58] Y.X. Wang, H.Q. Sun, H.M. Ang, M.O. Tade, S.B. Wang, Appl. Catal. B 164 (2015) 159–167.
[59] S. Indrawirawan, H.Q. Sun, X.G. Duan, S.B. Wang, J. Mater. Chem. A 3 (2015) 3432–3440.
[60] X.G. Duan, H.Q. Sun, Y.X. Wang, J. Kang, S.B. Wang, ACS Catal. 5 (2015) 553–559.